Batteries & Supercaps

Chemistry Europe
European Chemical Societies Publishing

Accepted Article

Title: New insights into Self-discharge and Heat Generation in Magnesium Batteries

Authors: Ijaz Ul Mohsin, Sibylle Riedel, Yanlei Xiu, Zhirong Zhao-Karger, and Carlos Ziebert

To be cited as: *Batteries & Supercaps* **2023**, e202300137

Link to VoR: https://doi.org/10.1002/batt.202300137

WILEY VCH

10.1002/batt.202300137

New insights into Self-discharge and Heat Generation in Magnesium Batteries

Ijaz Ul Mohsin*[1], Sibylle Riedel[2], Yanlei Xiu[2], Zhirong Zhao-Karger[2,3], Carlos Ziebert[1]

1. Institute of Applied Materials – Applied Materials Physics (IAM-AWP), Karlsruhe Institute of Technology, Karlsruhe, Germany
2. Helmholtz Institute Ulm (HIU), Helmholtzstrasse 11, 89081 Ulm, Germany, Karlsruhe Institute of Technology, Karlsruhe, Germany
3. Institute of Nanotechnology (INT), Karlsruhe Institute of Technology, P.O. Box 3640, 76021 Karlsruhe, Germany.

*Corresponding Author E-mail Address [ijaz.mohsin@kit.edu], Hermann-von-Helmholtz-Platz 1, 76344, Eggenstein-Leopoldshafen, Germany. Phone: +4972160823390, https://www.iam.kit.edu/awp/169.php

Abstract

Mo_6S_8 in the Chevrel Phase (CP) and 14-polyanthraquinone (14PAQ) cathode materials-based coin cells were assembled against Mg-foil as an anode by using 0.3 M magnesium tetrakis (hexafluoroisopropyloxy) borate $Mg[B(hfip)_4]_2$/dimethoxyethane (DME), 0.5 M $Mg[B(hfip)_4]_2$/DME and 0.5 M $Mg[B(hfip)_4]_2$/tetraglyme (G4) electrolytes. The heat generation of those three variants was compared using a sensitive MS80 Tian-Calvet calorimeter. The Chevrel Phase Mo_6S_8 was found to generate less heat than the organic 14PAQ. However, its specific capacity was also comparatively lower than for the organic cathode material. It is equally important for battery kinetics to have a well-designed electrolyte, therefore different solvents with the same electrolyte salt were utilized. Noticeable differences were observed and in tetraglyme solvent stable cycling and fewer self-discharge phenomena were detected. However, the activation process needs more cycles to achieve the required capacity in the case of the Chevrel Phase. The generated heat during cycling indicated the high resistances, swelling/contraction in organic cathodes leading to higher heat generation, and poor capacity retention. To overcome self-discharging in Mg batteries, side reactions/dissolution of cathode materials, electrolyte saturation and the formed interfaces on the anode side must be considered.

Keywords: Cell formation/activation, heat generation, electrolyte, self-discharging, impedance.

Introduction

The development of multivalent metal batteries has long been coveted as the next generation of sustainable batteries. Rock-forming elements such as magnesium, calcium, and aluminium

10.1002/batt.202300137

are geographically evenly distributed and in abundance. On account of increasing market demand, contemporary Li-ion batteries face material availability and sustainability concerns [1]. By doubling the number of electrons that are transferred per ion, divalent Mg-ion technologies can provide higher theoretical capacity and energy density than monovalent Li-ion batteries. A cell's theoretical voltage depends on the chemical potential difference between its anode and cathode [2]. The optimal anode material for Mg batteries is Mg metal, which has a low electrode potential (-2.4 V *vs.* SHE) and a high volumetric capacity of 3833 mAh.mL^{-1}. The Mg deposition also tends to form uniform structures and smooth surfaces [3] instead of highly dendritic structures as seen in the lithium and sodium depositions [4] [5]. However, the search for a suitable cathode material is more difficult due to the two steps involved in ion intercalation: ion diffusion and redistribution of divalent working ions [6] [7] . A primary limitation of high-voltage cathode materials is their low ionic diffusivity, caused by the strong electrostatic forces between the magnesium-ion and the cathode crystal matrix [8]. The need for energy storage systems that can meet the demands for safety, sustainability, high energy density, and high power has urged an increased interest in rechargeable Mg batteries. However, verification of their potential remains hindered by the availability of cathode material [9]. Despite tremendous efforts made towards the cathode development only very few of the proposed host structures are practically performing well and the benchmark in terms of ion mobility and cyclability, the Chevrel Phase Mo_6S_8 (CP), was reported more than 2 decades ago [10]. Mo_6M_8 phase (M = S, Se, Te) is an anionic phase that accommodates multivalent cations within the Mo6 framework [11]. At room temperature, CPs provide relatively fast and easy intercalation of Mg^{2+} ions, making them a popular cathode choice for magnesium batteries. Since Mo_6S_8 is a metastable phase at room temperature, it is indirectly stabilized by leaching the metal from the thermodynamically stable ternary Chevrel phase compounds, $MgMo_6M_8$ (M = S, Se, Te) [12]. Nevertheless, Mo_6S_8 has a theoretical capacity of 129 mAh g^{-1} and operates at less than 1.3 V vs. Mg^{2+}/Mg which is not appropriate for high-energy density energy storage systems. Consequently, magnesium-ion batteries need to focus on higher voltage and high-capacity cathode materials for the future. Therefore, organic-based cathodes have been considered as practicable alternatives to achieve high-energy, high-power Mg batteries because of their intrinsic high operating voltage and specific capacities [13] [14]. While inorganic crystal structures are generally dense and bonded by strong intermolecular forces, organic materials are loosely packed and provide energetically more favourable ionic pathways. These intrinsic properties draw the attention of scientists despite of their low electronic conductivity. There has been a great deal of interest in quinone-based compounds as they are thermodynamically advantageous in enolization reactions [13]. One example is polyanthraquinone sulfide (PAQS), but as a result of the high-capacity decay, PAQS cannot provide sustainable and long-term cycling performance. It is, however, still possible to improve the capacity retention of this type

10.1002/batt.202300137

of materials to make it an even more promising material for developing high-performance magnesium-ion batteries, especially by modification of the molecule and electrode structures. In the evaluation of three polyanthraquinone (PAQ) materials, namely 26PAQ, 15PAQ, and 14PAQ material for the magnesium batteries, it was found that rechargeable magnesium-ion batteries perform best with 14PAQ [15].

The safety measurements on magnesium batteries are currently missing in literature, because Mg-batteries are still at early stage i.e., at laboratory research level. In fact, safety data are a prerequisite for upscaling and for market acceptance; therefore, in this regard, thermal data based on CP and polyanthraquinone cathode materials were measured at coin cell level. In addition to being of scientific interest, it is also useful for commercial purposes to explore immoderate heat generation during electrochemical cycling. Heat generated during charging or discharging can accumulate inside the battery, affecting its performance and ageing, and causing unfavourable exothermal reactions, which can lead to thermal runaway [16] [17] . The MS80 Tian-Calvet calorimeter allows the direct measurement of heat flow in order to determine their heat generation during cycling. Using a 3D Tian-Calvet Sensor arrangement, hundreds of thermocouples form thermopiles around the sample and reference vessel, which determines heat flow. Consequently, heat flow values as low as 0.01 mW can be recorded [18]. The comparison was made on the activation process, cyclability, self-discharging and heat generation during the cycling procedure. The CR2032 coin cells were assembled based on Mo_6S_8, and 14PAQ as cathode vs Mg-foil as anode in the presence of 0.3 M magnesium tetrakis (hexafluoroisopropyloxy) borate $Mg[B(hfip)_4]_2$/dimethoxyethane (DME), 0.5 M $Mg[B(hfip)_4]_2$ /DME and 0.5 M $Mg[B(hfip)_4]_2$/tetraglyme(G4) electrolytes. The difference in electrochemical performance based on the different solvents for the electrolyte were investigated, and the corresponding heat generation was measured by a 3D-Calvet calorimeter.

Experimental:

Electrochemical studies:

The cathode slurry was a mixture of 90 wt. % commercial Mo_6S_8 (NEI Corp. USA), 5 wt.-% polyvinylidene fluoride binder (PVDF Solef 5130), 5 wt. % carbon black (C-NERGY Super C65) in N-methyl-2-pyrrolidon (NMP) solvent, which was mixed using a Speedmixer (Hauschild SpeedMixer® DAC 150). The slurry was coated with a doctor-blade on an aluminum current collector (20 µm) followed by drying (70 °C and 130 °C) and calendaring. Self-synthesis 14PAQ@Ketjenblack (14PAQ@KB) composite cathode [19] was prepared by mixing 95 wt. %

10.1002/batt.202300137

composite (mass ratio, 14PAQ : Ketjenblack = 2 : 1) plus 5 wt.% sodium alginate in water and coated on an aluminum foil following by drying at 60°C overnight under vacuum (10^{-3} bar). The obtained coated electrode sheet had an active mass loading (14PAQ) of 1.5 mg.cm-². This cell is later named as 14PAQ-coated cells throughout the manuscript. The 14PAQ cell in reference [16] is named as 14-PAQ-pressed material cell, as the author investigated a cathode which was pressed onto an aluminium mesh in the cell casing and not in the form of a coated sheet.

The prepared Mo_6S_8 cathode sheet had an active mass loading of 3.64 mg/cm². The reason to have a bit higher active material powder loading is to assemble a CR2032 coin cell with sufficient capacity that can produce a detectable heat flow signal in the calorimeter. The positive electrode Mo_6S_8 of 15 mm diameter and pure polished-Mg metal (15 mm diameter disc) as anode were implemented in CR2032 coin cells by adding 150 µl of 0.3 M $Mg[B(hfip)_4]_2$ /dimethoxyethane (DME), 0.5 M $Mg[B(hfip)_4]_2$/DME and 0.5 M $Mg[B(hfip)_4]_2$/tetraglyme(G4) electrolyte solutions and two glass fiber separators (Whatman GF/A). The cells were cycled in a battery tester (Biologic EC-Lab, MPG 2) at 25 °C (Binder incubator) within the operating voltage window of 0.5 – 1.8 V. The cycling stability tests were performed at a C-rate of 0.2 C (charge / discharge) with a constant current profile with respect to the cathode mass loading. The same procedure was repeated for 14PAQ coin cells (14 mm diameter cathode and 14 mm Mg metal anode). Table 1 summarizes the electrolytes and electrodes combination used in the current investigation of coin cells.

Table 1: The combinations of the coin cells ingredients

Cathode	Electrolyte	Anode
Mo_6S_8	0.3 M $Mg[B(hfip)_4]_2$ /dimethoxyethane (DME)	Mg foil
Mo_6S_8	0.5 M $Mg[B(hfip)_4]_2$/tetraglyme(G4)	Mg foil
14PAQ (pressed material)	0.5 M $Mg[B(hfip)_4]_2$/DME	Mg foil
14PAQ (coated material)	0.5 M $Mg[B(hfip)_4]_2$/tetraglyme(G4)	Mg foil

Using the Biologic EC-Lab (MPG 2) cycler, EIS measurements were made on the coin cells at state of charge (SOC) 100% with sequential relaxation time of 1h with the following test parameters: frequency range = 20 kHz – 10 mHz, single sine mode, potential perturbation / sinus amplitude = 10 mV, points per decade = 6 at a temperature of 25 °C.

Thermal characterization:

The pristine formatted CR2032 coin cells from Mo_6S_8 with ~0.3 mAh and 14PAQ (coated) with ~0.26 mAh capacity were mounted in the coin cell holders and isolated with ceramic tape to inhibit a short circuit. The coin cell holders were attached to the cycler (BioLogic BCS) with wires outside the MS80 Tian-Calvet calorimeter. There are four channels in the MS80 calorimeter, two sample channels and two reference channels, each measuring 32 mm in

diameter. It is possible to perform two coin cell tests in parallel in that type of calorimeter. The complete experimental set-up was already mentioned in a previous paper [20]. For equalizing the mass in the reference and sample chambers, dummy coin cells with the same geometry and weight were placed into each reference channel. The related cycling data during the calorimetric experiment were recorded via a BioLogic instrument (BCS) with the constant current (CC) test profile both in charging (1.8 V) and discharging (0.5 V) with a rate of 0.17 C in case of CP and 0.2C at 25 °C with charging/discharge voltage window of 2.5-0.5 V in case of 14PAQ. Each charge and discharge cycle were separated by a 10 h relaxation time to acquire thermal equilibrium.

Post-mortem investigation

After 200 cycles the cycle-aged electrodes have been taken out from the coin cells at full discharge state (SOC 0%) and rinsed with DME and tetraglyme (G4) solvents, respectively. After drying at 60 °C for 48 h under vacuum (10^{-3} mbar), scanning electron microscopy SEM (Thermo Fischer Phenom XL) and Energy-dispersive X-ray spectroscopy (EDX) were made at these electrodes to investigate the changes in surface morphology and interfaces in comparison to the pristine electrodes.

Results and discussions:

Formation/activation process

The formation/activation of freshly assembled coin cells was conducted with 0.1 C rate (with respect to cathode mass loading) by constant current and constant voltage (CCCV) profile. The large overpotential in the first cycle could be originating from the electrochemically inactive species adsorbed on the Mg surface [21] and is probably due to the elimination of a thin MgO oxide layer on the Mg anode (although Mg metal was scratched to remove the oxide layer) or the reduction of some impurities during the initial cycles. In subsequent cycles, CP in DME shows some humps which are indicating the formation of some interphases on the Mg metal anode or-/and on the cathode (Figure 1a). According to Tutusaus et al., [21] and Zhao Karger et al., [22] the initial Mg plating process exhibits a high impedance as a result of an electrochemically inactive adsorption layer on the electrode surface. Our analysis also suggests that Mg surface oxides (impurities) may also contribute to overpotentials. The stable reversible storage for CP in DME of Mg^{2+} is achieved with a capacity of 50 mAh.g^{-1} after 10 activation cycles with a Coulombic efficiency of (CE) of 95%. Irreversible capacity refers to the reduction of impurities and trace moisture in electrolytes, or other side reactions in cells components. On the contrary, in the solvent G4, due to its increased viscosity, which may reduce the mobility of the ions during the initial 10 cycles as for the DME solvent, less activation on the anode side is observed (figure 1b). Thus, further cycles (e.g., 20 more cycles (figure

10.1002/batt.202300137

1C)) are required to achieve a complete activation. Remarkable differences that are observed are i) that there is no humps formation and ii) cycles with a Coulombic efficiency of almost 100% (Figure 1c) are obtained. High reversible plating/stripping of the Mg anode is an essential factor for evaluation of the electrolyte performance especially in metal anode batteries.

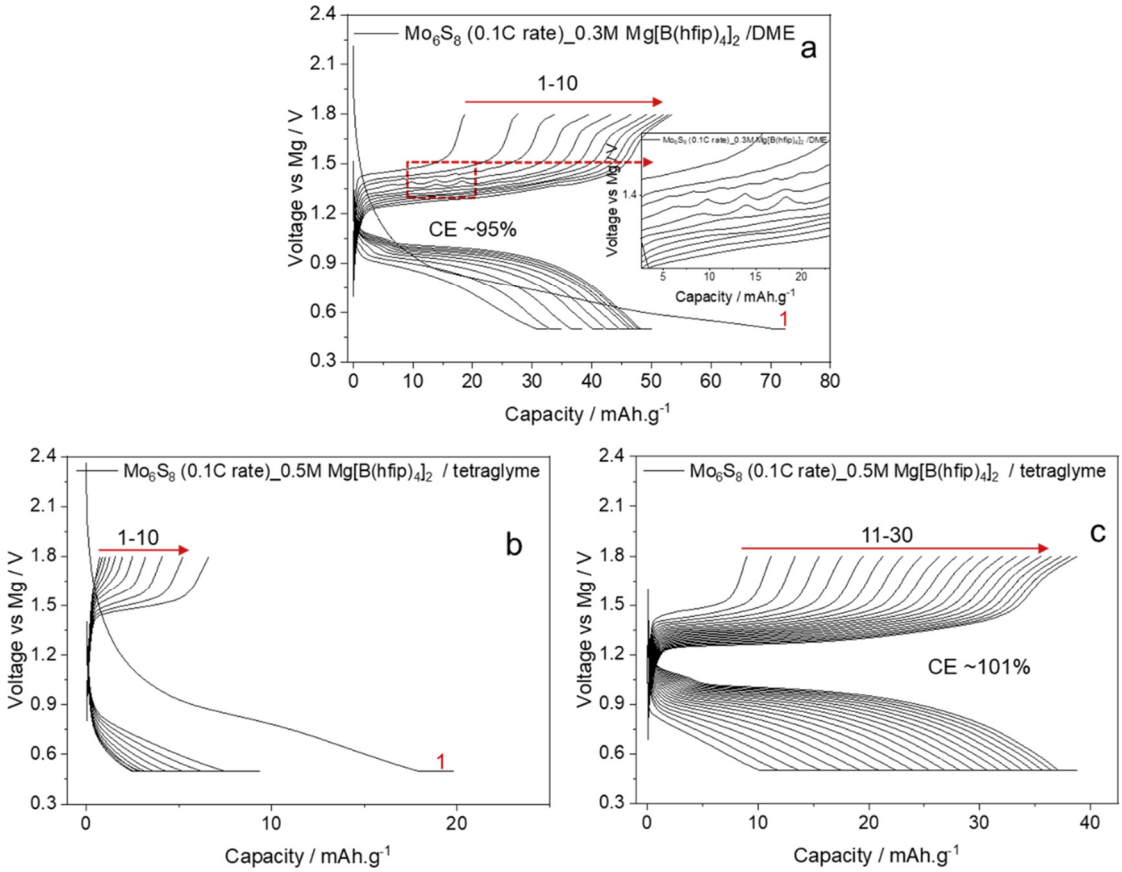

Figure 1: Comparison of the voltage vs. capacity curves during formation/activation of coin cells (a) first 10 cycles for Mo_6S_8 in DME solvent, (b) first 10 cycles for Mo_6S_8 in G4 solvent, (c) additional 20 cycles for Mo_6S_8 in G4 solvent.

The Chevrel phase (CP) is a standard intercalation cathode material used in Mg batteries to benchmark performance. The electrochemical performance of $Mg[B(hfip)_4]_2$ was compared both in DME and G4 solvents (figure 2a and b). Mg||Chevrel phase cells containing the $Mg[B(hfip)_4]_2$/G4 electrolyte demonstrate a better Coulombic efficiency and lower overpotentials. After 30 activation cycles, the capacity of this cell stabilizes at around 50 $mAh{\cdot}g^{-1}$, which is similar as for the cell containing the $Mg[B(hfip)_4]_2$/DME electrolyte. A distinct difference is observed in the shape of the discharge voltage plateau. An observable voltage plateau at 1.18 V indicates a reduced trapping of Mg^{2+} ions inside Mo_6S_8 and better utilization of the second site for Mg^{2+} ion insertion inside the structure. Both coin cells containing DME and G4 are cycled up to 200 cycles with a charge/discharge rate of 0.2 C and

10.1002/batt.202300137

are presented up to state of health (SOH) 80% in figure 2c. In comparison to DME, G4-containing cells show more stable cycling. However, due the viscous solvent, G4 shows poor rate capability and exhibits ~40 mAh·g^{-1} capacity initially and until 200 cycles manifests 20% of capacity fading. Conversely, cells containing DME solvent exhibit ~46 mAh·g^{-1} of initial capacity and deplete to SOH of 80% within 100 cycles. The Coulombic efficiency (CE) for both systems stayed stable throughout the cycling and is given in figure 2c. With 98.3%, G4 shows a higher Coulombic efficiency than the DME containing solvent cell, which reaches 95.5%. Since the initial 10 cycles are executed in heat generation test, cyclability tests started from cycle number 10 (figure 2c). In cyclability test, the Mg plating/stripping overpotentials were reduced and were well maintained near approx. 0.2 V for 200 cycles.

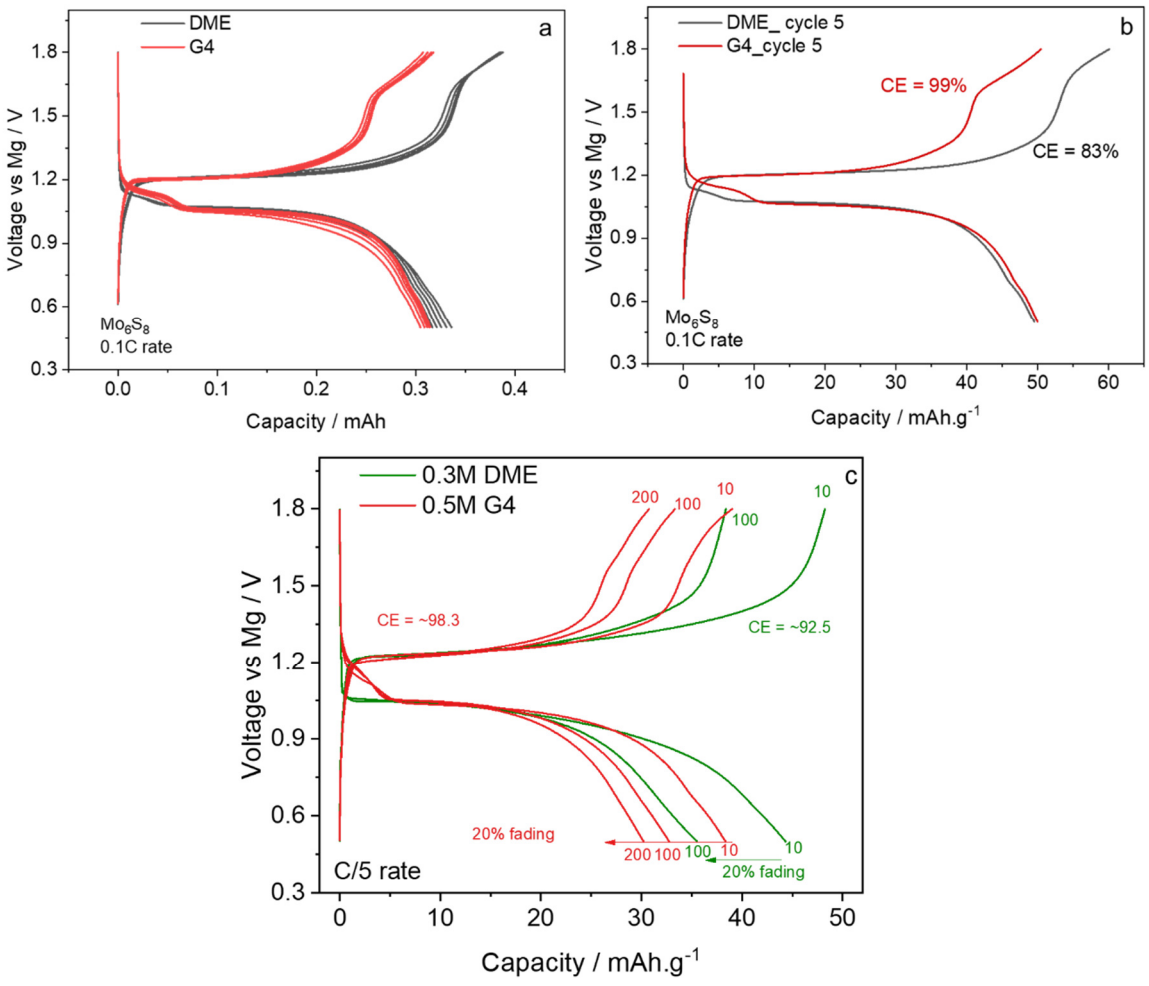

Figure 2: comparison of Mo_6S_8 in DME and G4 electrolyte solvents; (a) last 5 formation-cycles of Mo_6S_8 in different electrolytes, (b) comparison of 5th cycles of Mo_6S_8, (c) cyclability test of Mo_6S_8 in DME and G4.

In the next step, the electrochemical performance of $Mg[B(hfip)_4]_2$ electrolyte in G4 solvent with 14PAQ cathode was tested (figure 3). These cathode materials undergo different

10.1002/batt.202300137

electrochemical reactions with Mg^{2+} ions through different mechanisms of reversible enolization reaction of carbonyl functional groups [23] rather than intercalation as in case of CP. As a model system among the anthraquinone categories, 14-polyanthraquinone (theoretical capacity of 260 mAh·g^{-1}) cathodes exhibit reasonable reversibility and initially show medium-capacity in Mg cells of around 100 mAh·g^{-1} (with 0.1C rate) after activation/formation of ~20 cycles (figure 3a), followed by a stable cycling with 0.2C rate (figure 3b). Xiu et al.[19] have evaluated the electrochemical performance of the 14PAQ-pressed cathode in DME electrolyte solvent using coin cells with voltages between 0.5 and 2.5 V. The formation/activation process needed more cycles to achieve the required specific capacity than for the G4 based system in the current scenario. In their studies, in the initial cycling stability test, DME based electrolyte showed unsatisfactory capacity retention, with a sharp discharge capacity drop from 240 to150 mAh·g^{-1} within 100 cycles. In the subsequent 400 cycles, it exhibited a less pronounced capacity fading, i.e., 150 to 78 mAh·g^{-1}. In the present work, the performance of Mg cells using 14 PAQ cathode employing $Mg[B(hfip)_4]_2$/G4 electrolytes is very similar to CP in G4 in terms of Coulombic efficiency (Figure 3 a,b). However, the initial capacity in G4 solvent is half of the DME based electrolyte. This leads to the possible explanation that the two adjacent carbonyl groups could only accommodate one inserted magnesium cation species due to steric hinderance resulting from the chelating interaction [15] during the activation process on the 14PAQ cathode. Hence, the stabilized capacity of 14PAQ is only half of its theoretical capacity, which agrees with experimental observation. However, with regard to the capacity decay in the cyclability test, the 14PAQ cell with G4 overperforms DME, reaching still around 60 mAh·g^{-1} after 200 cycles. A clear difference can be observed in terms of cell's overpotential, where again $Mg[B(hfip)_4]_2$/G4 exhibits slightly lower overpotential throughout the cycling procedure. Overall, the reversibility of 14PAQ-coated electrodes in Mg cells is good. However, 14PAQ-pressed suffers from larger capacity decay, which could be explained by polymer swelling and partial dissolution of the active mass in cells containing non-concentrated/unsaturated electrolyte [19].

10.1002/batt.202300137

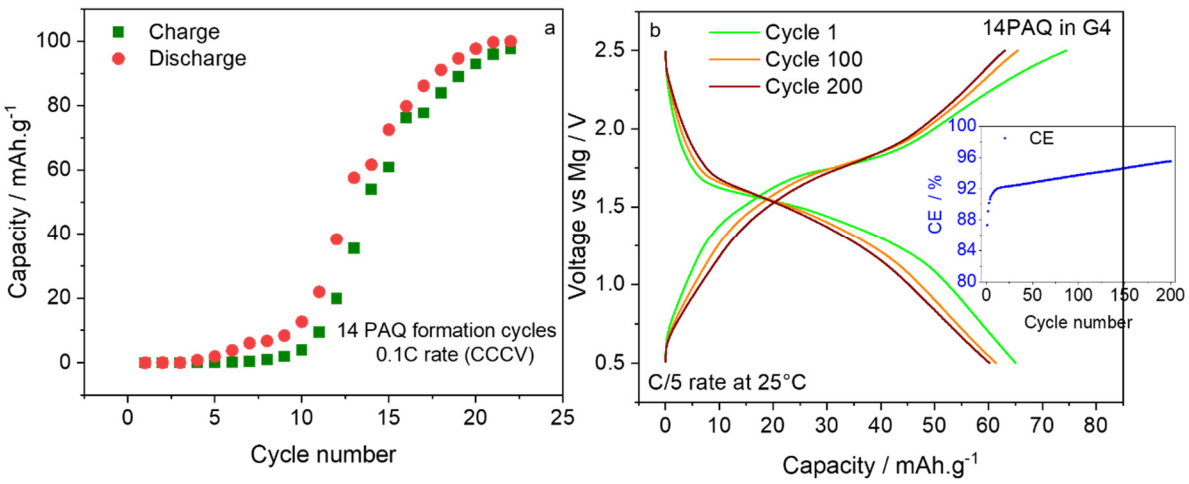

Figure 3: (a) activation / formation cycles of 14PAQ-coated in G4, (b) cyclability test of 14PAQ in G4

As reported in literature, impurities including water, dissolved gases, and solvent stabilizers can adversely affect the electrochemical performance of electrolytes for Mg batteries in terms of plating/stripping efficiency and cell's overpotential [24]. The cyclability test of 14PAQ-coated cathode material in G4 shows excellent electrochemical performance and a capacity fading of around 10% until 200 charge/discharge cycles with 0.2C rate (figure 3b). The related coulombic efficiency is below 90% at the start, gets better with subsequent cycling (sub-figure 3b) and exhibits a low-voltage polarization as well. Thus, the 14PAQ-coated in G4 outperforms the 14PAQ- pressed in DME, even if the initial capacity of the latter is significantly higher. The reactivity of the metal surface could be reduced by using additives during plating and stripping on magnesium metal [25].

Heat generation

The voltage, current and heat flow rate curves of Mo_6S_8 in DME and G4 that have been recorded during the calorimetric experiment with a current rate of C/7 at 25 °C are presented in figure 4a and 4b for two representative cycles. The blue curves show the cell voltage, the current is represented by the red curves and the corresponding heat flow signal is given by the green curves. Figure 4c shows the generated heat per capacity ($J{\cdot}mA^{-1}h^{-1}$) that has been determined by integration over the heat flow curves. There is a clear increase in heat flow rate throughout discharge at increased rates of discharge due to the higher irreversible heat generation, since the internal resistances for both systems also increase with the increase in the state of the charge as has been found out during the EIS measurements. Nevertheless, for SOC 50% lower values have been determined, as depicted in figure 4d. The iR drop at various SOCs levels, e.g., SOC0%, SOC50% and SOC100% is measured and internal resistances are calculated (figure 4d). SOC has been found to affect the internal resistance of

10.1002/batt.202300137

cells and is associated with heat generation. As SOC decreases, diffusion resistance and charge transfer increase. Since entropy heat is reversible and diffusion rate mechanism is limiting in de-magnesiated state, it is highly dependent on SOC. The internal resistance of the DME system is higher at SOC0% which also corresponds to the total generated heat. i.e., at the start of charging, the heat flow rate is higher in DME than in G4. However, a sharp increase in heat flow rate is observed at SOC 100% which can be attributed to an increase in the internal resistance to 7 kΩ in DME and 6 kΩ in case of G4 which results in an increase in the heat flow rate near the end of discharge/charge [26]. The heat generation at different C-rates was also measured and is presented in the supplementary figures S1 and S2. As the rate capability of the system in G4 is not as high as in DME, low specific capacities for faster charging/discharging rates have been measured due to the high viscosity of G4 (figure S1 & S2).

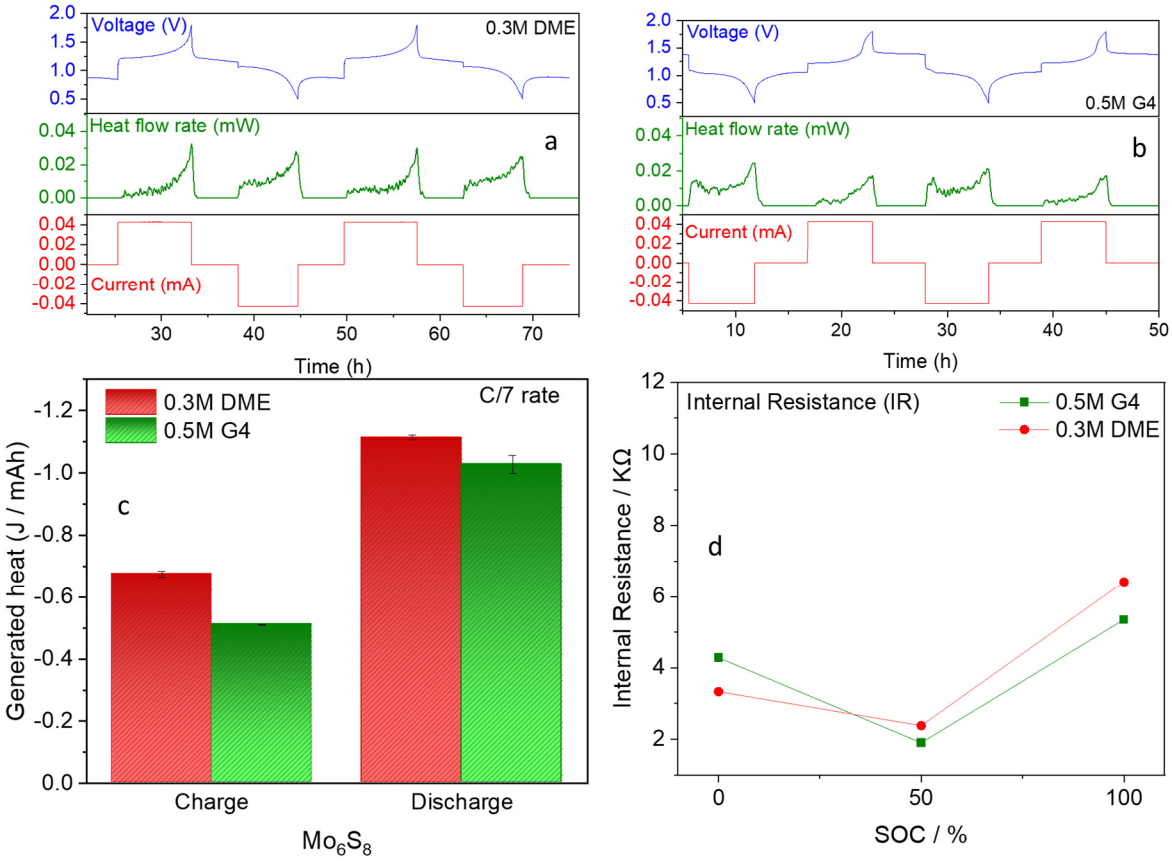

Figure 4: (a) voltage, current and heat flow rate curves of Mo_6S_8 in DME, (b) voltage, current and heat flow rate curves of Mo_6S_8 in G4, (c) corresponding capacity-normalized generated heat for both systems for C/7 charge/discharge rate, d) Dependence of internal resistance on SOC for Mo_6S_8 in G4 and DME.

10.1002/batt.202300137

The complex impedance of these two systems at SOC100% was also measured by electrochemical impedance spectroscopy and was fitted by an equivalent circuit model (ECM) to obtain the different resistances as shown in figure 5. In Figure 5a and figure 5b illustrate the variations in charge transfer resistance caused by the solid interfacial layer (R3) and adsorption layer (R2) respectively. In the Nyquist plots in figure 5a and 5b, the shape of the fitted semi-circles is different and a distinctly pronounced semi-circle is observed in the G4 solvent, which reveals the formation of a stable solid electrolyte interphase (SEI). In addition, electrochemical impedance spectroscopy (EIS) observed the growth of impedance values for both electrolytes during the rest time (figure 6). An increase in the resistance of the solid electrolyte interphase (SEI) layer indicates that the layer has been stabilized (figure 6a). This is one of the reasons for the observation that less self-discharging occurs in G4 containing electrolyte (figure 8b, which will be discussed later in the section 3.3 self-discharge). After each 1 h rest time, R2 and R3 in G4 solvent contributed more to the total impedance than CP in DME solvent (figure 6a and 6b). However, R3 decreases slightly first and then later during a rest time of 5 h back to 26 kΩ which is almost equal to the initial value after 1 h relaxation, suggesting a growth of the adsorption layer under static conditions. R2 (in figure 6b) which represents the charge-transfer resistance due to the solid electrolyte interphase (SEI) increases gradually from 12 Ω to 16 Ω in DME solvent, although the comparative resistances R2 and R3 over relaxation time are very small in DME solvent. In comparison, the change in R3 over relaxation time was negligible, indicating a good chemical compatibility between both electrolytes and the Mg anode in G4 solvent. On the other hand, the R3 value for DME based electrolyte is comparatively 10 times lower, showing an unstable system, which also can be seen in the self-discharging behavior of the DME based system (figure 7a). As the layer grows, self-discharge will decrease correspondingly with increasing interphase thickness [27]. The self-discharging phenomenon is indicating the dissolution of interphases while resting [28] [29]. Although the addition of the $Mg(BH_4)_2$ additive to the electrolyte decreases significantly the R3 value as reported in [30], by removing the thin oxide layer on the fresh Mg anode. The migration barrier is higher and the Mg-ion mobility becomes rather difficult in the presence of MgO and MgF_2 interfaces on the anode (Mg-foil) [31]. These interfaces are observed more frequently in the DME based system, as is shown and discussed in the section 3.4 on post-mortem analysis. The ohmic heat is related to long range interactions, i.e., Joule heating from electron and ionic flow resistance within the electrodes and the electrolyte, contact resistance and solid electrolyte interphase (SEI) resistance. The kinetic heat is related to the charge-transfer reactions at the interphase. The mass transport heat refers to mass transport limitations in the electrodes or the electrolyte.

10.1002/batt.202300137

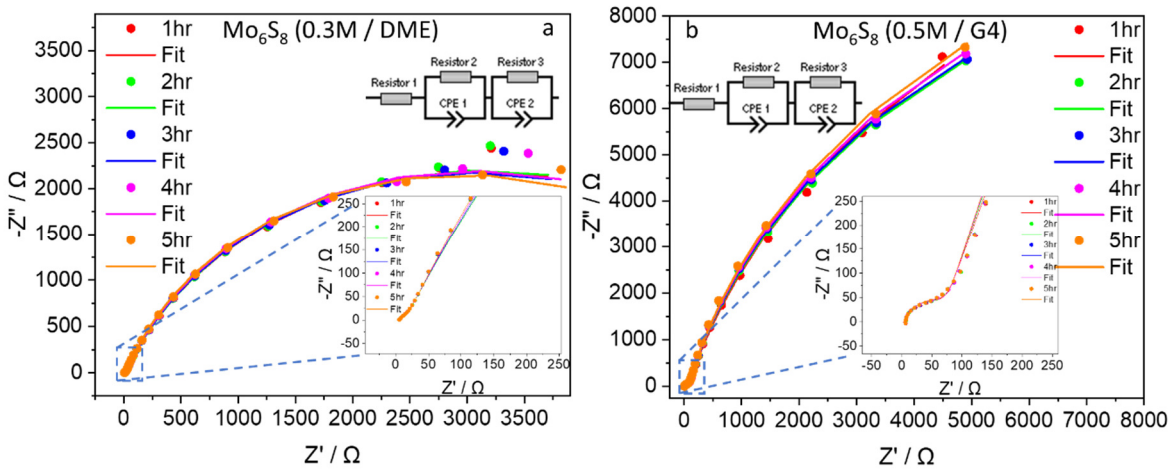

Figure 5: Nyquist plots of Mo_6S_8 at SOC100%: (a) in DME, (b) in G4

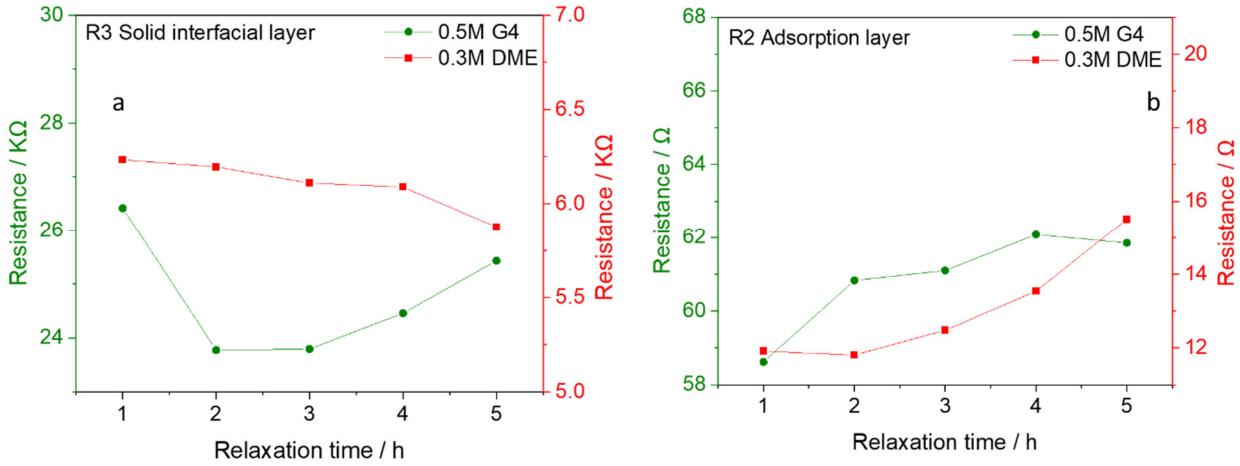

Figure 6: Equivalent circuit model parameters derived from the fitting of the EIS results; (a) solid interfacial passivation layer (R3), (b) adsorption layer (R2) over the relaxation time.

In similar manner, the heat generation is determined both on 14PAQ-coated cells with G4 solvent in the electrolyte and 14PAQ-pressed cells from the previous study [19] with DME solvent. The voltage, current and heat flow rate curves of the two systems are presented in figure 7a and 7b for two representative cycles. The blue curves show the cell voltage, the current is represented by the red curves and the corresponding heat flow signal is given by the green curves. Figure 7c shows the generated heat per capacity ($J \cdot mA^{-1}h^{-1}$) that has been determined by integration over the heat flow curves for a 0.2 C rate at 25°C. The generated heat in these organic based 14PAQ cells is found surprisingly distinct for the pressed-14PAQ cell (figure 7c). A notable fact is that it exhibits a negative heat flow signal during charging (figure 7b), indicating that the cell absorbed heat (endothermic reaction) during the magnesium extraction. The take-up heat occurs by entropy change during de-magnesiation, and entropy changes are responsible for the heat absorption associated with material phase changes in

10.1002/batt.202300137

the cell. Based on generated heat results, it is evident that pressed 14PAQ cell containing DME solvent electrolyte shows significantly reduced heat generation as compared to coated-14PAQ cell containing G4 solvent. However, it is challenging to upscale the pressed material methodology to the commercial level. The galvanostatic charge-discharge curve of pressed-14PAQ cells are shown in supplementary figure S3 with and without relaxation of 10 h. The Coulombic efficiency (CE) reduces from 95% to 85% with the introduction of 10 h relaxation time which is a clear indication of self-discharge of this material in DME solvent. The heat generation of pressed-14PAQ in DME solvent at a high C-rate of 1.0C is also provided in supplementary figure S4. The decrease in discharge capacity is observed due to 10% of self-discharge during 10 h relaxation time. as indicated by the Coulombic efficiency (figure S3). The higher coulombic efficiency CE due to the thickening of SEI layers indicates the slowing of parasitic reactions between electrodes and electrolytes that cause the CE to depart from unity [32]. As long as the batteries have the same test history, those with higher Coulombic efficiency (CE) should have a longer lifespan, which is proven in current studies in the case of the cyclability test.

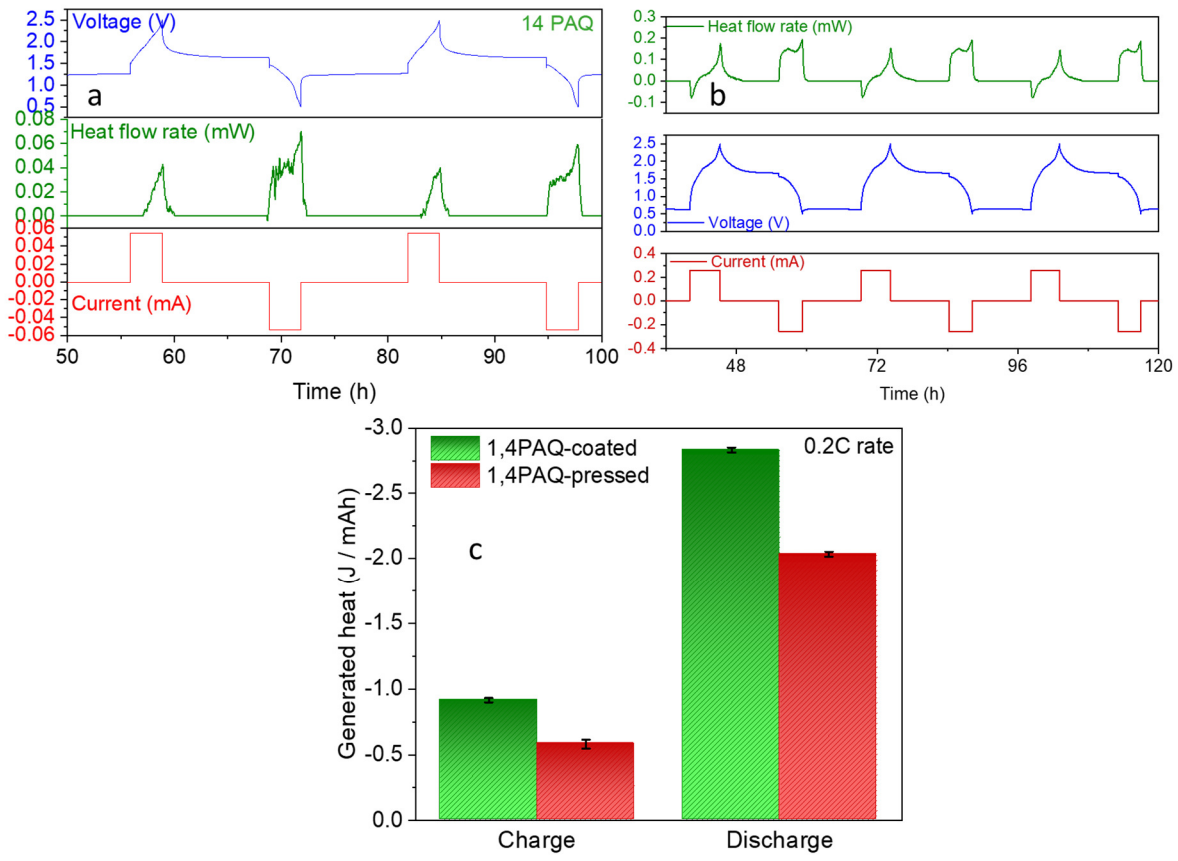

Figure 7: (a) voltage, current and heat flow rate curves of 14PAQ coated on Al foil in G4 solvent, (b) voltage, current and heat flow rate curves of 14PAQ pressed on Al foil in DME solvent, (c) corresponding capacity-normalized generated heat with 0.2 C rate.

10.1002/batt.202300137

Self-discharge

The self-discharge behavior was analyzed in all systems discussed above. The respective pristine coin cells are charged and discharged with respective C-rates (0.1 C and 1.0 C) for 2-3 cycles and then hold for 24 h at the fully charged state. Afterwards, the coin cells are discharged with the same C-rate and then charged and discharged again for 2-3 cycles to determine the Coulombic efficiency as shown in figure 8 for the two CP cells. Undesirable parasitic chemical reactions cause a cells available capacity (stored energy) to be spontaneously and irreversibly reduced by self-discharge without any external connection. The self-discharge is higher in DME based solvent with 23% as given in terms of the Coulombic efficiency. Conversely, G4 system shows a better stability, and it reveals only 3% of self-discharge due to the saturated electrolyte and interphases that do not dissolve into the electrolyte (figure 8b). Both systems are tested with a higher rate of 1C to see the influence of the fast charging/discharging on the self-discharge. The similar trend is observed i.e., no noticeable difference was found (supplementary figures S4 and S5).

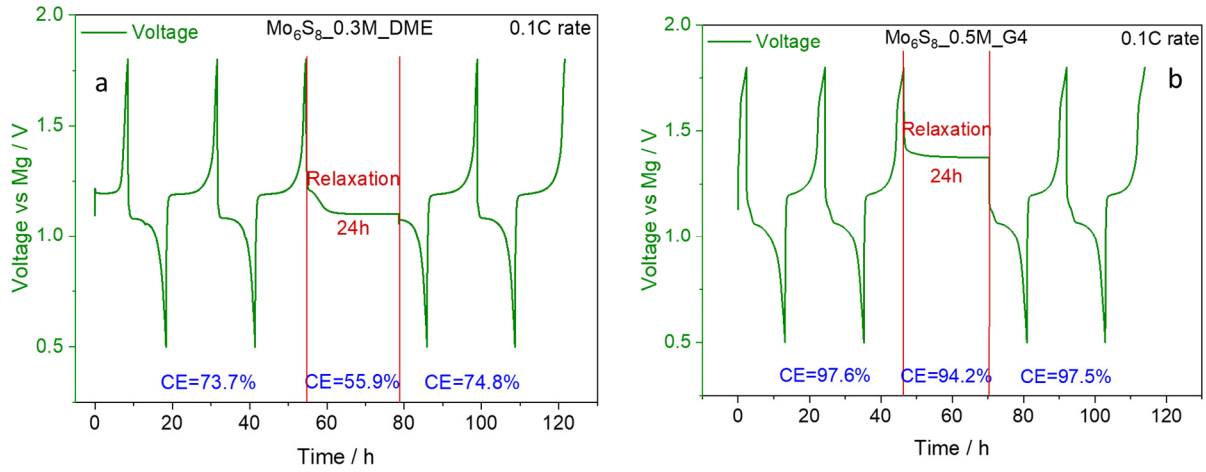

Figure 8: self-discharge (a) Mo_6S_8 in DME, (b) Mo_6S_8 in G4 with 0.1 C rate

The self-discharge of Mg||14PAQ in DME (pressed material) and G4 (coated material) was also investigated. Similar results are obtained as those for the CP material. The 14PAQ-pressed material in coin cell shows 36% of self-discharge during a relaxation period of 24 h in DME based electrolyte (figure 9a). The 14PAQ coated material on an aluminium foil in the coin cell turns out to be very stable in G4 solvent and the Coulombic efficiency only decays by 4% over 24 h (figure 9b). Organic cells discharge by natural phenomena that are driven by the same forces that permit them to operate [33]. Several chemical reactions occur at the electrode interface between active masses, auxiliary materials, and electrolyte-solutions as well as shuttle processes across the ionically conducting phase between the electrodes, which contribute to self-discharge [34].

10.1002/batt.202300137

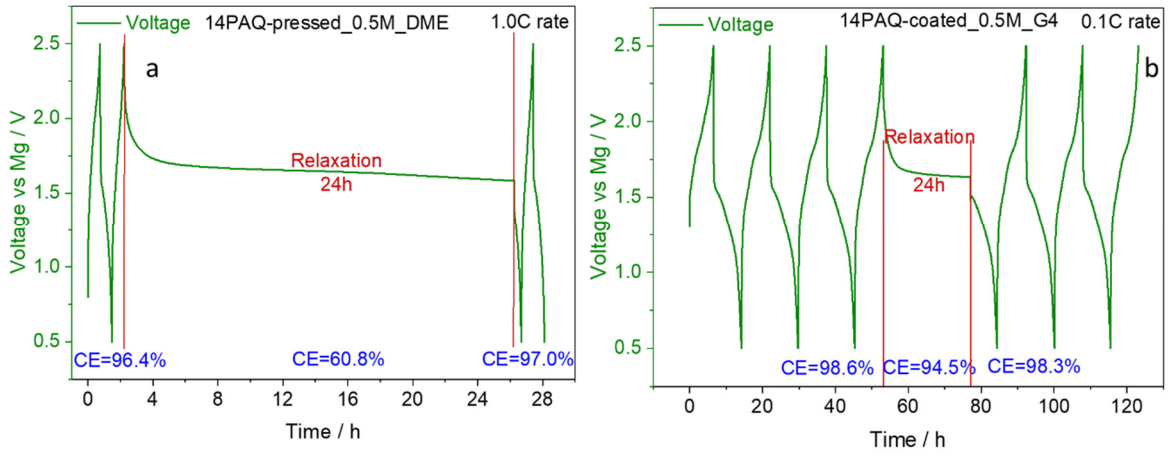

Figure 9: self-discharge (a) 14PAQ-pressed in DME with 1.0 C rate, (b) 14PAQ-coated in G4 with 0.1 C rate

Post-mortem analysis

In addition to the Coulombic efficiency (CE), the morphology and composition of the deposited film on the anode also play a crucial rule to the cycle life of Mg batteries. The scanning electron microscopy (SEM) images of the Mg anode surface after 200 cycles are compared with that of a pristine (polished) Mg-foil to investigate the interface morphology between the anode and electrolyte. Although the surface appears uneven in different cycle-aged Mg-anodes, no significant sharp feature resembling dendrites are found (figure 10), which is very important to deliver high energy density and for safe operation of Mg batteries. Compared to the pristine Mg-foil, the surface morphology of the cycle-aged Mg anodes, shown in figure 10 (b, c, d), appears porous. Energy dispersive X-ray (EDX) measurement shows that besides magnesium, carbon (C), fluorine (F), and oxygen (O) are present in small amounts, but no boron (B). The EDX spectrum and elemental mapping (figure 11) of the sample in DME confirms that the MgO/or and organofluoride -CF_2/-CF_3/MgF_2 deposition on Mg metal anode exists in higher concentration with elements, such as C, O, F. The concentration of C, O, F of each cycle-aged anodes are presented in table S1 (supplementary table). The higher concentration of C, and F is found in cycle-aged anode in DME. Based on the XPS measurements by Roy et al., [35] it can be assumed that this is most probably not a result of the MgF_2 based solid interphase. Further investigation of such thin solid interphases will require high-resolution transmission electron microscopy (HR-TEM). Nevertheless, the SEM/EDX images of cycle-aged Mg-anode provide some evidence of formation of interphase and porous surfaces hint the dissolution of these interphases into the electrolyte. The porous surface of cycle-aged Mg anode against Mo_6S_8 in DME is studied with point-EDX measurement to know the elemental composition and shown in supplementary figure S6. A high concentration O and

10.1002/batt.202300137

C contents inside the porous area was observed indicating the thinner interfaces and subsequently the dissolution into the electrolyte leading to the porous, uneven morphology.

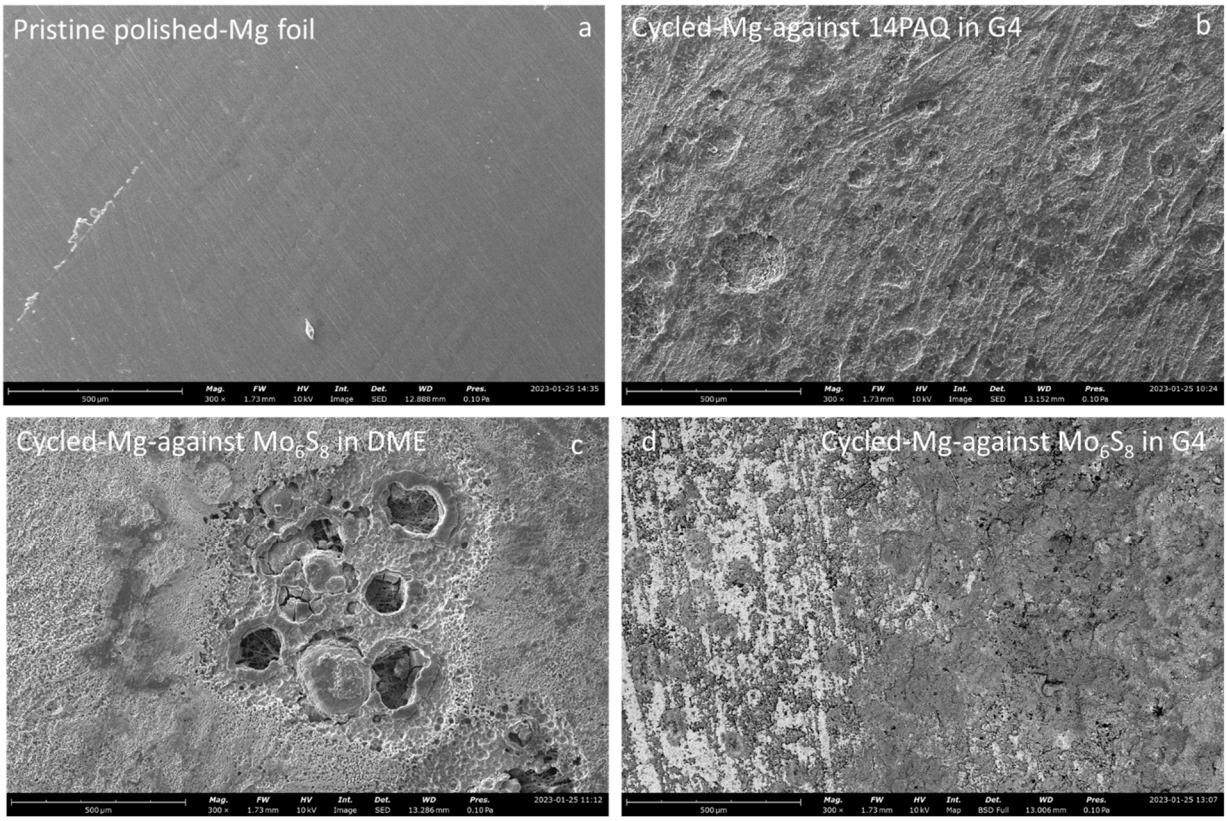

Figure 10: (a) morphology of pristine polished-Mg anode, (b) morphology of cycle-aged (200 cycles) Mg anode against 14PAQ in G4, (c) morphology of cycle-aged (200 cycles) Mg anode against Mo_6S_8 in DME, (d) morphology of cycle-aged (200 cycles) Mg anode against Mo_6S_8 in G4.

10.1002/batt.202300137

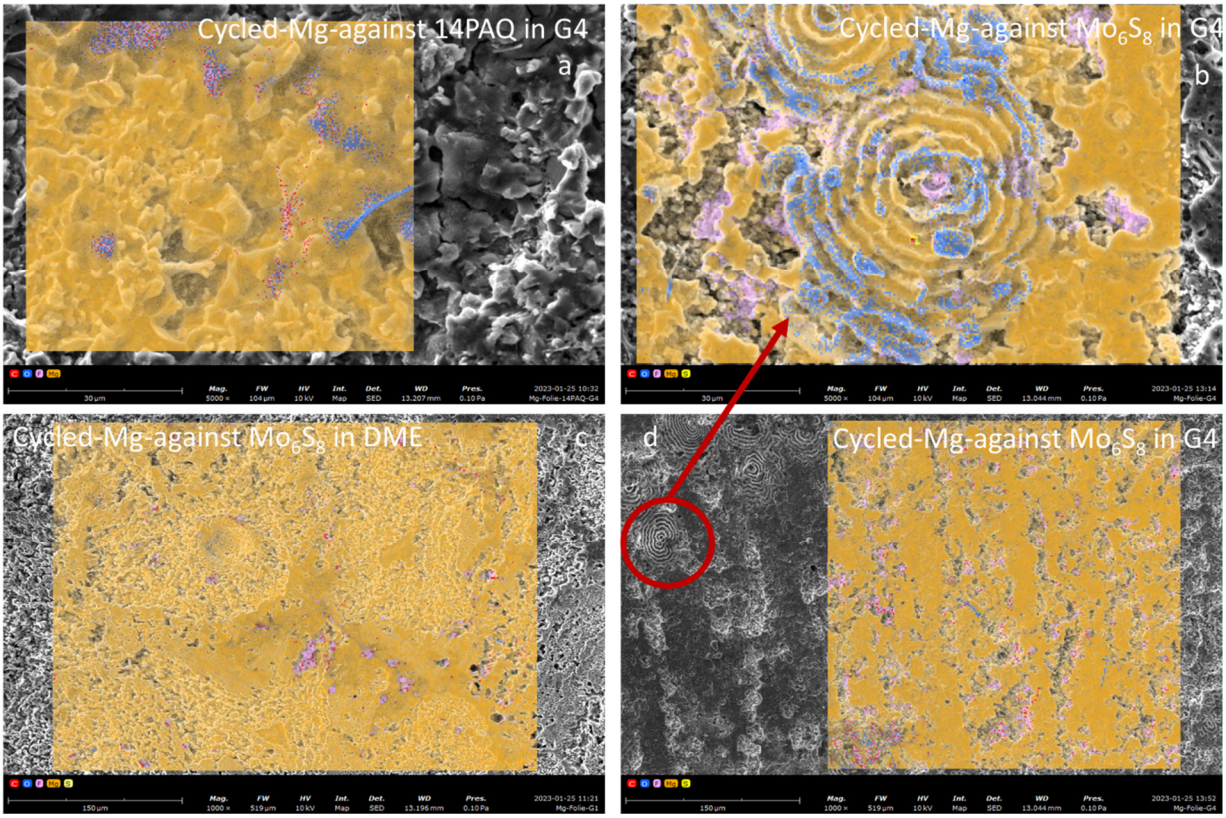

Figure 11: EDX-elemental mapping of (a), cycle-aged (200 cycles) Mg anode against 14PAQ in G4, (b) zoomed circled area of cycle-aged (200 cycles) Mg anode against Mo_6S_8 in G4 (c) cycle-aged (200 cycles) Mg anode against Mo_6S_8 in DME, (d) cycle-aged (200 cycles) Mg anode against Mo_6S_8 in G4.

The noticeably spiral shape microstructures on some spots are seen in Mg-anode in G4 (vs Mo_6S_8) as zoomed-in/highlighted in figure 11b. The elemental mapping of such spiral pattern shows comparatively more O and F contents, indicating the formation of magnesium oxide and probably fluoride. The blue and pink colors represent O and F element maps, respectively.

Conclusions and outlook

Detailed results of a study have been presented on the functioning and performance of different magnesium full coin cells using commercial Mo_6S_8 in the Chevrel Phase (CP), self-synthesized 1,4-polyanthraquinone (14PAQ) cathodes against Mg-foil by utilizing 0.3 M magnesium tetrakis (hexafluoroisopropyloxy) borate $Mg[B(hfip)_4]_2$ /dimethoxyethane (DME), 0.5 M $Mg[B(hfip)_4]_2$ /DME and 0.5 M $Mg[B(hfip)_4]_2$ /tetraglyme(G4) electrolytes. The following conclusions can be drawn:

- In G4 solvent stable cycling and fewer self-discharge phenomena, however activation process needs more cycles to achieve the required capacity.

- Less heat is generated at a low C-rate in the case of G4 and better electrochemical performance is achieved.
- The electrochemical heat generation rate is a strong function of the current and SOC, with increases near the end of charge / discharge for high and low SOCs.
- Internal resistance changes with the state of charge and is higher in the case of 0.3 M DME. The generated heat during the cycling phases indicated the high resistance.
- Side reactions/dissolution of formed interfaces on the anode side must be considered.

To find the anode interface species that have been dissolved into the electrolyte, an analysable amount of electrolyte after cycling is required, which is not possible to extract in case of coin cell level. Therefore, in future upscaling to pouch cell level will be studied, for which the amount of electrolyte is in the millilitre (mL) range and the electrolyte can be extracted using a centrifuge for a subsequent investigation by analytical techniques e.g., High-performance liquid chromatography (HPLC) or gas chromatography mass spectrometry (GC-MS). Additionally, thermal abuse tests on pouch cell level to identify the exothermal reactions of respective cells will also be performed.

Acknowledgment

The authors gratefully acknowledge Ms. Alexandra Reif for her assistance with the SEM-EDX analysis. This work contributes to the research performed at CELEST (Center for Electrochemical Energy Storage Ulm-Karlsruhe) and was funded by the German Research Foundation (DFG) under Project ID 390874152 (POLiS Cluster of Excellence, EXC 2154).

Conflicts of Interest: The authors declare no conflict of interest.

Reference

[1] C. European, I. E. Directorate-General for Internal Market, Smes, S. Bobba, S. Carrara, J. Huisman, F. Mathieux, C. Pavel, *Critical raw materials for strategic technologies and sectors in the EU : a foresight study*, Publications Office, **2020**.
[2] G. Ceder, M. K. Aydinol, A. F. Kohan, *Comput. Mater. Sci.* **1997**, *8*, 161-169.
[3] M. Jäckle, A. Groß, *J. Chem. Phys.* **2014**, *141*, 174710.
[4] D. Aurbach, Y. Cohen, M. Moshkovich, *Electrochem. Solid-State Lett.* **2001**, *4*, A113.
[5] V. Kumar, Y. Wang, A. Y. S. Eng, M.-F. Ng, Z. W. Seh, *Cell Rep. Phys. Sci.* **2020**, *1*, 100044.
[6] E. Levi, M. D. Levi, O. Chasid, D. Aurbach, *J. Electroceram.* **2009**, *22*, 13-19.
[7] E. Levi, Y. Gofer, D. Aurbach, *Chem. Mater.* **2010**, *22*, 860-868.
[8] F. Thöle, L. F. Wan, D. Prendergast, *Phys. Chem. Chem. Phys.* **2015**, *17*, 22548-22551.
[9] R. Mohtadi, O. Tutusaus, T. S. Arthur, Z. Zhao-Karger, M. Fichtner, *Joule* **2021**, *5*, 581-617.
[10] D. Aurbach, Z. Lu, A. Schechter, Y. Gofer, H. Gizbar, R. Turgeman, Y. Cohen, M. Moshkovich, E. Levi, *Nature* **2000**, *407*, 724-727.

[11] E. Levi, A. Mitelman, O. Isnard, M. Brunelli, D. Aurbach, *Inorg. Chem.* **2008**, *47*, 1975-1983.
[12] P. Rabiller, M. Rabiller-Baudry, S. Even-Boudjada, L. Burel, R. Chevrel, M. Sergent, M. Decroux, J. Cors, J. L. Maufras, *Mater. Res. Bull.* **1994**, *29*, 567-574.
[13] Z. Zhao-Karger, M. Fichtner, *Front. Chem.* **2019**, *6*.
[14] H. Dong, Y. Liang, O. Tutusaus, R. Mohtadi, Y. Zhang, F. Hao, Y. Yao, *Joule* **2019**, *3*, 782-793.
[15] B. Pan, J. Huang, Z. Feng, L. Zeng, M. He, L. Zhang, J. T. Vaughey, M. J. Bedzyk, P. Fenter, Z. Zhang, A. K. Burrell, C. Liao, *Adv. Energy Mater.* **2016**, *6*, 1600140.
[16] H. Yang, S. Amiruddin, H. J. Bang, Y. K. Sun, J. Prakash, *J Ind. Eng. Chem.* **2006**, *12*, 12-38.
[17] R. Spotnitz, J. Franklin, *J. Power Sources* **2003**, *113*, 81-100.
[18] I. U. Mohsin, C. Ziebert, M. Rohde, H. J. Seifert, *J. Electrochem. Soc.* **2021**, *168*, 050544.
[19] Y. Xiu, Z. Li, V. Bhaghavathi Parambath, Z. Ding, L. Wang, A. Reupert, M. Fichtner, Z. Zhao-Karger, *Batteries Supercaps* **2021**, *4*, 1850-1857.
[20] I. U. Mohsin, L. Schneider, M. Häringer, C. Ziebert, M. Rohde, W. Bauer, H. Ehrenberg, H. J. Seifert, *J. Power Sources* **2022**, *545*, 231901.
[21] O. Tutusaus, R. Mohtadi, N. Singh, T. S. Arthur, F. Mizuno, *ACS Energy Lett.* **2017**, *2*, 224-229.
[22] Z. Zhao-Karger, R. Liu, W. Dai, Z. Li, T. Diemant, B. P. Vinayan, C. Bonatto Minella, X. Yu, A. Manthiram, R. J. Behm, M. Ruben, M. Fichtner, *ACS Energy Lett.* **2018**, *3*, 2005-2013.
[23] Y. Xiu, A. Mauri, S. Dinda, Y. Pramudya, Z. Ding, T. Diemant, A. Sarkar, L. Wang, Z. Li, W. Wenzel, M. Fichtner, Z. Zhao-Karger, *Angew. Chem., Int. Ed.* **2023**, *62*, e202212339.
[24] I. Shterenberg, M. Salama, H. D. Yoo, Y. Gofer, J.-B. Park, Y.-K. Sun, D. Aurbach, *J. Electrochem. Soc.* **2015**, *162*, A7118.
[25] J. G. Connell, B. Genorio, P. P. Lopes, D. Strmcnik, V. R. Stamenkovic, N. M. Markovic, *Chem. Mater.* **2016**, *28*, 8268-8277.
[26] T. M. Bandhauer, S. Garimella, T. F. Fuller, *J. Electrochem. Soc.* **2011**, *158*, R1.
[27] B. R. Thomas, *Linden's Handbook of Batteries, Fourth Edition*, 4th ed. ed., McGraw-Hill Education, New York, **2011**.
[28] D. Aurbach, M. Moshkovich, A. Schechter, R. Turgeman, *Electrochem. Solid-State Lett.* **2000**, *3*, 31.
[29] D. Aurbach, A. Schechter, M. Moshkovich, Y. Cohen, *Journal of The Electrochemical Society* **2001**, *148*, A1004.
[30] Z. Li, T. Diemant, Z. Meng, Y. Xiu, A. Reupert, L. Wang, M. Fichtner, Z. Zhao-Karger, *ACS Appl. Mater. Interfaces* **2021**, *13*, 33123-33132.
[31] M. Sotoudeh, A. Groß, *J. Phys. Chem.* **2022**, *13*, 10092-10100.
[32] B. Gyenes, D. A. Stevens, V. L. Chevrier, J. R. Dahn, *J. Electrochem. Soc.* **2015**, *162*, A278.
[33] J. B. Schlenoff, J. C. W. Chien, *Synth. Met.* **1988**, *22*, 349-363.
[34] R. Holze, *Adv. Mater. Sci. Technol.* **2022**, *4*, 32-47.
[35] A. Roy, V. Bhagavathi Parambath, T. Diemant, G. Neusser, C. Kranz, R. J. Behm, Z. Li, Z. Zhao-Karger, M. Fichtner, *Batteries Supercaps* **2022**, *5*, e202100305.

10.1002/batt.202300137

Table of Contents (ToC) entry (a.k.a. graphical abstract)

The comparison is made on the activation process and cyclability of magnesium cells. The first-time total heat generation and self-discharging analysis of the Chevrel Phase Mo_6S_8 and organic 14PAQ in different electrolytes are measured. The heat generation in magnesium coin cells mechanisms are elucidated. The self-discharging in different electrolyte solvents is explained and the dissolution of interphases is indicated.

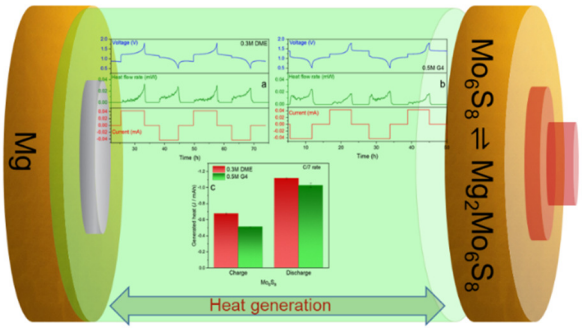

Twitter: Please provide all relevant Twitter handles at the end of the document below the ToC entry (personal or institutional).

https://twitter.com/ClusterPolis